

COBALT NEWS

PUBLISHED BY THE COBALT DEVELOPMENT INSTITUTE

08/2

April 08

2 Comment

3 2007 Production Statistics

5 Ultra-High-Strength Steels Vs Titanium Alloys

8 *THE* Cobalt Conference

9 Nanoparticles Unlock the Future of Superalloy Metal

11 The Trade-Offs and Economics in Functional Grades

COBALT NEWS

CHAIRMAN

S. Dunmead (OM Group, USA)

VICE CHAIRMEN

D. Morgan (QNI, Australia)
T. Shepherd (Shepherd Chemicals, USA)

DIRECTORS

I. Akalay (CTT, Morocco)
S. Brown (Chambishi Metals, Zambia)
G. Chen (Xiamen Tungsten, China)
G. Dyason (Xstrata Nickel, Canada)
J. Gullberg (Sandvik, Sweden)
W. Hsu (Kennametal, Inc., USA)
P. Jeanpetit (Eurotungstène, France)
T. Kubota (Sumitomo MM, Japan)
R. Martin (Shu Powders, China)
D. McIntyre (Vale Inco, Canada)
C. Tan (WMC, Canada)
M. Vydra (ICCI, Bahamas)
C. Zyde (Umicore, Belgium)

THE COBALT DEVELOPMENT INSTITUTE

167 High Street, Guildford, Surrey, GU1 3AJ, UK

Tel: (0)1483 578877 Fax: (0)1483 573873

e-mail: info@thecdi.com

Website: www.thecdi.com

Editor: D. Weight – Production: I. Porri

ISSN: 1353-5587

The Cobalt Development Institute carries out activities from a head office in Guildford, UK, to promote the use of cobalt. It is legally incorporated as an association of a wholly non-profit making character in accordance with its memorandum and articles, which are available on request. Membership of the CDI is open to those engaged or interested in the industry, by application and acceptance by the Board.

Cobalt News exists to disseminate promotion material on uses for, and development in, cobalt technology supported by items of interest to cobalt producers, users and all their customers. Unless otherwise stated as copyright reserved, Cobalt News permits the reprint of articles if fully credited to Cobalt News and its contributors where appropriate.

Comment is the responsibility of the Editor. Views expressed by the contributors are their own. Neither

COMMENT

In this edition of the Cobalt News we include a review of production statistics for 2007 and, following a year when availability of refined cobalt has once again been constrained by the supply of raw material, it is encouraging to note that refined production availability has stabilised from the reduction observed in 2006.

From information provided to the CDI, it can be observed that refined cobalt availability has remained roughly the same as the previous year at 53,700 tonnes. However, demand is also strong and we have seen historically high prices of over US\$50/lb recorded this year.

We are aware that there are several cobalt projects coming on stream to meet the growing demand and we await news of these developments and what effect this will have on the market.

Of course, information is the key to understanding such developments and what better place to obtain this than from *THE* Cobalt Conference which the CDI is holding in Toronto in May 2008. Registrations for this year's conference are particularly good and you are advised to book soon to ensure a place. Please see our website for details.

necessarily reflect those of the Institute, its directors or its members. Material is presented for the general information of the reader, and whilst believed to be correct, the CDI, its members, staff and contributors do not represent or warrant its suitability for any general or specific use and assume no liability of any kind in connection with the provision of the said information.

The Cobalt Development Institute is registered at 167 High Street, Guildford, Surrey, GU1 3AJ.

2007 Production Statistics

Production

The CDI estimates that total cobalt supply in 2007, from the main sources reporting their production, was 53,723 tonnes, which roughly the same as availability in the previous year. This compares to a 2.2% fall in refined production in 2006 when compared to 2005. Table 1 illustrates refined cobalt production from CDI members for calendar years 2001-2007

It can be seen that production from CDI members fell by 1,067 tonnes (or -3.18%) in 2007 to 32,470 tonnes as compared to 2006. Reductions were re-

Member companies	2001	2002	2003	2004	2005	2006	2007
BHPB, Australia	1818	1863	1800	1900	1400	1600	1800
CTT, Morocco	1200	1354	1431	1593	1613	1405	1591
Eramet France	199	176	181	199	280	256	305
ICCI, Canada	2943	3065	3141	3225	3391	3312	3573
Norilsk, Russia	4600	4200	4654	4524	4748	4759	3587
OMG, Finland	8100	8200	7990	7893	8170	8580	9100
Sumitomo, Japan	350	354	379	429	471	920	1084
Umicore Belgium ⁽²⁾	1090	1135	1704	2947	3298	2840	2825
Vale Inco, Canada	1450	1480	1000	1562	1563	1711	2031
Xstrata (Norway)	3314	3993	4556	4670	5021	4927	3939
Zambia ⁽¹⁾	2789	4344	4570	3769	3648	3227	2635
Total	27853	30164	31406	32711	33603	33537	32470

(1) Chambishi Metals. (2) Includes Umicore's Chinese production

corded by Norilsk, Xstrata, Chambishi and to a much lesser extent Umicore. All other CDI Members recorded increases in production, particularly OMG who are now incorporating the Norilsk cobalt units after the arrangement made between the companies last year. In particular, Eramet increased production by almost 20%, Sumitomo by 18% (as the Coral

Bay, Philippines project further develops), Vale Inco by 19% and significant other increases were recorded for BHPB, CTT and ICCI-Sherritt. Production increases can also be ascribed to the continued buoyancy of the nickel market and increased activity in this sector.

Refined cobalt availability from other sources is outlined in Table 2. Total refined

Non-Member companies	2001	2002	2003	2004	2005	2006	2007
Bulong	203	200	0	0	0	0	0
China ⁽³⁾	1470	1842	4576	8000	12700	12700	13245
Gecamines, DRC	3199	2149	1200	735	600	550	606
India	250	270	255	545	1220	1184	980
Kasese, Uganda	634	450	0	457	638	674	698
Minara, Australia	1452	1838	2039	1979	1750	2096	1884
Mopani Copper, Zambia ⁽⁵⁾	1876	1800	2050	2022	1774	1438	1800
South Africa ⁽⁴⁾	252	256	285	300	214	257	275
Votorantim, Brazil	889	960	1097	1155	1136	902	1148
CIS	0	0	0	0	0	0	0
Total	10225	9765	11502	15193	20032	19801	20636
Other Sources of Supply							
DLA Deliveries	1896	1284	1987	1632	1199	294	617
Other Stockpile Releases	0	0	0	0	0	0	0
Non-Members Total	12121	11049	13489	16825	21231	20095	21253

(3) Excludes Umicore production. (4) Estimate for Nov & Dec. (5) Estimate for 2007

production from these non-CDI members increased by 4.2% compared with 2006 to 20,636 tonnes from 19,801 tonnes.

Table 3 – Total Refined Cobalt Availability (Tonnes)							
	2001	2002	2003	2004	2005	2006	2007
CDI Members	27853	30164	31406	32711	33603	33537	32470
Others	12121	11049	13489	16825	21231	20095	21253
TOTAL	39974	41213	44895	49536	54834	53632	53723

Even though cobalt concentrate imports to China were some 26% lower than 2006, Chinese cobalt producers were able to record a 4.3% increase in refined cobalt production. It was also noted that raw cobalt carbonate imports increased to 13,000 tonnes, which to some extent compensated for the reduction in concentrates. In addition there has been a higher utilisation of cobalt containing intermediates in that market. Therefore Chinese production shows an increase to 13,245 tonnes compared to 12,700 tonnes in 2006. It is emphasised that the figure for China excludes Umicore's Chinese production which is already included in Table 1.

Votorantim's Tocantins operation performed well during the year and recorded an impressive 27% increase in production to 1,148 tonnes for 2007. Gécamines, DRC and Kasese, Uganda also recorded increases compared to the previous year. The CDI has estimated that Mopani, Zambia have been able to improve production despite the current problems with electrical power capacity in the region. Decreased production was apparent in India mainly as a result of a shortage of raw material. Minara also recorded a reduction of cobalt production at Murrin Murrin in Australia, but the total compares with variations observed in previous years. DLA deliveries during 2007 were 617 tonnes which was 323 tonnes higher than in 2006. Including DLA deliveries, total availability of cobalt from other sources was 21,253 tonnes, some 1,158 tonnes (or 5.76%) higher than in 2006. At 31 December 2007,

the DLA stockpile stood at about 676 tonnes.

A summary of total refined cobalt availability from 2001 to 2007 is shown in Table 3. It can be seen that overall availability in 2007 totalled 53,723 tonnes, some 91 tonnes higher than in 2006.

As in the past, we emphasise that the figures do not include production of refined cobalt from companies treating various cobalt-containing intermediate products and scrap who do not report their numbers to the CDI.

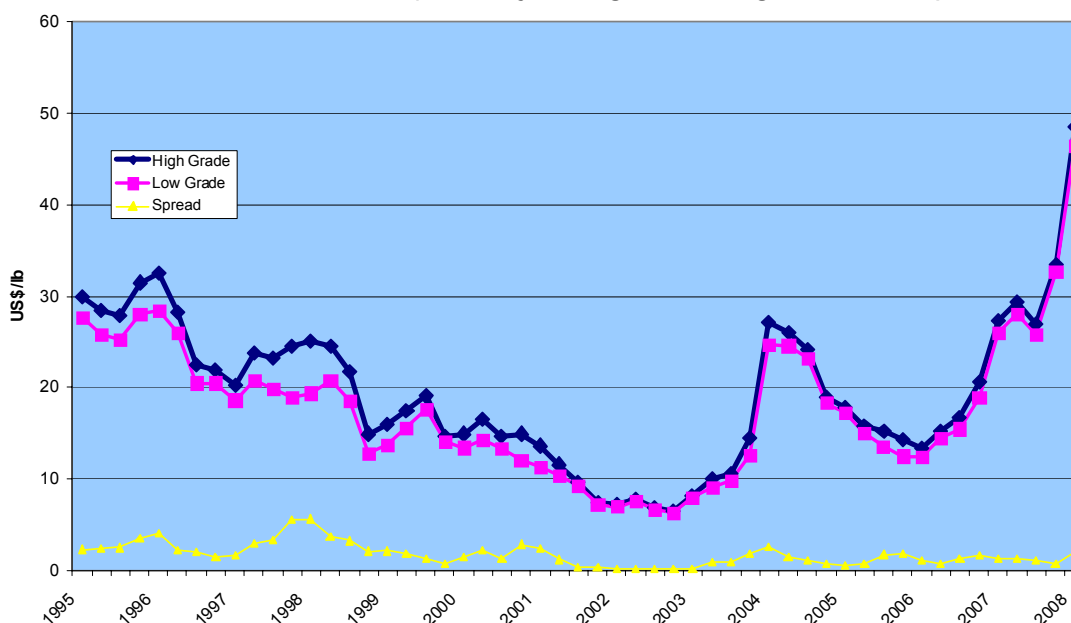
Demand

The CDI has published supply and demand data in the WBMS/CDI book "World Cobalt Statistics" for 2004-2006. These data were derived from worldwide import/export figures. The publication can be purchased from either the CDI or the WBMS. Figures for 2007 will be available in the next few months. See this website for details.

Price

The graph below illustrates the change seen in the average quarterly Metal Bulletin free market price quotation for cobalt since 1995 for 99.8% and 99.3% min. cobalt. Based on quarterly averages, the graph does not show short-term price fluctuations.

Cobalt Price 1995-2008 (Quarterly Averages including 1st Quarter 08)



ULTRA-HIGH-STRENGTH STEELS VS TITANIUM ALLOYS

This study compares the strength, ductility, toughness and fatigue properties of AerMet alloys, maraging steels and titanium.

The range of ultra-high-strength steels with good toughness has expanded in recent years to allow more alloy choices. In addition to maraging steels, another family of ultra-high strength steels that possess outstanding toughness has been developed to meet the same demanding service requirements.

This article discusses evolution of the newer AerMet alloy family, then compares those steels with maraging steels and titanium alloys. Relative strength, ductility, toughness and fatigue properties of the three groups are described in detail, showing that the AerMet alloys have better fatigue life and overall better combinations of strength and toughness than either the maraging steels or titanium alloys.

Family evolution

The AerMet 100 alloy was developed in response to a need from McDonnell Douglas and the U.S. Navy for a stronger and tougher material for the landing gear of the F/A 18 E/F fighter aircraft. The Navy wanted an alloy that could be a drop-in replacement for 300M, but with twice the fracture toughness. The AerMet 100 alloy met the Navy's requirements with its minimum ultimate tensile strength of 280 ksi (1930 MPa) and minimum fracture toughness of 100 ksi√in.



A cloud builds up around an F/A-18C Hornet as it breaks through the sound barrier above the Pacific Ocean.

AerMet 100 was followed by higher-strength derivatives such as the 875°F-Aged AerMet 100 alloy and the AerMet 310 alloy, which has minimum ultimate tensile strength of 310 ksi (2137 MPa). Another AerMet alloy development program was undertaken because it appeared that even higher strength alloys could be designed. That effort led to the development of AerMet 340 alloy, which has a 340 ksi (2344 MPa) minimum UTS.

Physical metallurgy

Nominal composition listed in Table 1 Show that the AerMet alloy family and the 18Ni maraging steels are closely related chemically.

Table 1 – Nominal compositions (wt%) of the ultra-high-strength/high-toughness maraging steels and AerMet alloys

Element	18 Ni maraging family			AerMet family		
	Marage 250	Marage 300	Marage 350	AerMet 100	AerMet 310	AerMet 340
C	0.03 max.	0.03 max.	0.05 max.	0.23	0.25	0.33
Cr	0.50 max.	—	0.25	3.1	2.4	2.25
Ni	18	18.5	18	11.5	11	12
Mo	5	5	4.2	1.2	1.4	1.85
Cu	0.50 max.	—	0.15	—	—	—
Co	7.5	9	12.25	13.5	15	15.6
V	—	—	0.04	—	—	—
Ti	0.4	0.6	1.7	0.015 max.	0.015 max.	0.015 max.
Al	—	—	—	0.015 max.	0.015 max.	0.015 max.
B	—	0.003 Add	0.003	—	—	—
Zr	—	0.02 Add	0.01	—	—	—
Ca	—	0.05 Add	0.05	—	—	—

Table 2 – Structure and heat treatment of ultra-high-strength/high-toughness alloys

	18Ni maraging family	AerMet family
Structure		
Type of structure	Precipitation hardened	Precipitation hardened
Matrix	Low C, Fe-Ni lath martensite	Low C, Fe-Ni lath martensite
Strengthening mechanism	Ni ₃ Mo, Ni ₃ Ti, Ni ₃ (Mo,Ti); FeMo, FeTi, Fe(Mo,Ti) precipitates	(Mo, Cr) ₂ C carbides
Heat Treatment		
Hardening or solution temperature	1500°F (816°C)	1625 to 1775°F (885 to 968°C)
Quench	Air	Air or Oil
Refrigeration	No	-100°F (-73°C), 1 h
Age	900°F (482°C), 3 to 8 h	825 to 925°F (441 to 496°C), 3 to 8 h

Table 2 compares the physical metallurgy of both alloy families, which both have a structure that consists of a low-carbon, Fe-Ni-Co lath martensite matrix that is age-hardened. However, the precipitates that age-harden the alloys are different.

The 18Ni maraging steels are hardened through the precipitation of intermetallic compounds, primarily Ni₃Mo, Ni₃Ti, and Ni₃(Ti, Mo). On the other hand, the AerMet alloys are strengthened through the precipitation of (Mo, Cr)₂C carbides. Fig. 1 shows the typical microstructure of AerMet 100.

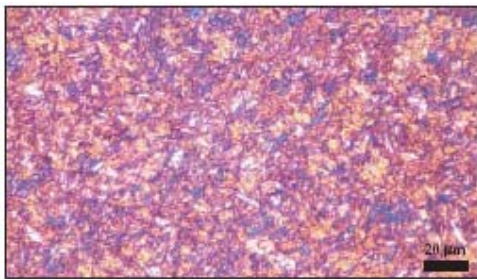


Fig. 1 – Microstructure of AerMet 100 Alloy. Courtesy George Vander Voort, Buehler Ltd

Design criteria

Designers often have other criteria for evaluating alloys before they make a choice based on mechanical properties. Some of these criteria are space limitations, corrosion resistance, service temperature, magnetic properties, and cost.

Because of density differences, parts made from the AerMet alloys and maraging steels have an advantage over titanium alloys in that they occupy a smaller envelope than parts made from a titanium alloy. However, with their inherent corrosion resistance, titanium alloys have an advantage over ultra-high strength steels that do not contain significant chromium or other elements that impart stainless behaviour. These steels are frequently plated or coated to prevent rusting in aerospace applications.

Titanium alloys also can operate at higher temperatures than the AerMet alloys and maraging steels. In addition, titanium alloys are not magnetic, while the ultra-high strength steels are magnetic.

Finally, price can be a consideration. Raw material prices have been fluctuating a great deal in recent years and, in general, titanium alloys can be more expensive than either the AerMet alloys or maraging steels.

Mechanical properties

The two most preferred titanium alloys, Ti-6Al-4V and Ti-10V-2Fe-3Al, were chosen for comparison with the AerMet alloys and maraging steels in this study. Many sources were consulted for data to determine average mechanical properties of the AerMet alloys, the maraging steels, and the titanium alloys.

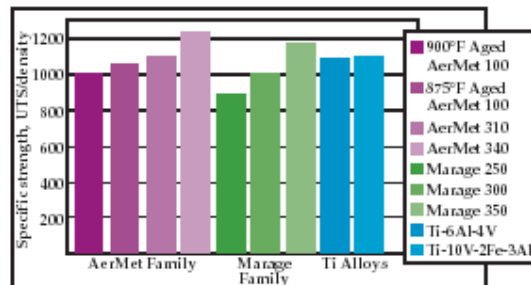


Fig. 2 — Specific strength comparison.

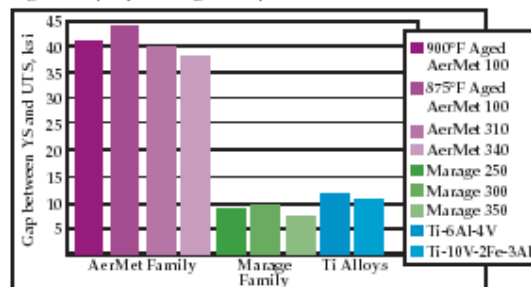


Fig. 3 — Comparison of the gap between yield strength (YS) and ultimate tensile strengths (UTS).

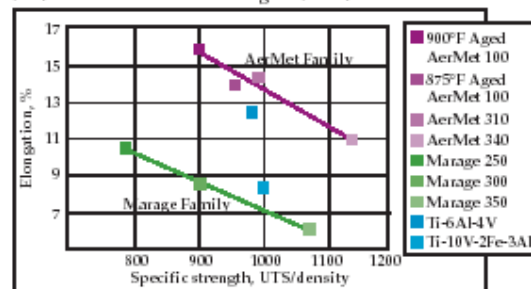


Fig. 4 — Elongation vs. specific strength.

Table 3 – Mechanical properties of the alloy families

Property	900°F Aged AerMet 100	875°F Aged AerMet 100	AerMet 310	AerMet 340	Marage 250	Marage 300	Marage 350	Ti 6Al-4V	Ti 10V-2Fe-3Al
Ultimate tensile strength, ksi	287.0	302.0	315.0	352.0	258.6	291.0	343.6	173.5	185.0
Yield strength, ksi	246.0	258.0	275.0	314.0	249.9	281.6	336.4	162.0	174.5
Elong., %	16.0	14.0	14.5	11.0	10.7	8.6	6.1	12.5	8.5
Reduction in area, %	67.0	64.0	63.0	55.0	51.1	40.8	22.2	52.0	17.5
Charpy V-notch impact energy, ft-lb	35.0	30.0	20.0	11.0	20.5	18.5	10.0	18.5	22.0
Fracture toughness K _{Ic} , ksi-in. ^{1/2}	120.0	99.0	65.0	32.0	91.5	67.7	38.5	39.1	49.6
Density, lb/in. ³	0.285	0.285	0.288	0.284	0.289	0.289	0.292	0.16	0.168
Fatigue strength 10 ⁷ cycles, ksi	137	137	150	143	110	128	112	102	120
Specific strength, UTS/density	1007	1060	1094	1239	895	1007	1177	1084	1101

To make a graphical comparison simpler, average values were used rather than value ranges. However, this approach does have disadvantages, mainly because the maraging steels individually exhibit wide ranges for each of the tensile properties depending on product size and heat treatment. For example, the average yield and tensile strengths for Marage 250 listed in Table 3 are 249.9 and 258.6 ksi, respectively. These averages were calculated based on values ranging from 245.0 to 269.1 ksi for yield strength, and 251.0 to 279.0 ksi for ultimate tensile strength.

The average mechanical properties of all the alloys are listed in Table 3 and graphically compared in Fig. 2 through 8. To make valid property comparisons, an effort was made to account for the density differences between the titanium alloys and the two families of ultra-high-strength steels.

Therefore, the specific strength (ultimate tensile strength/density) was used to compare properties of the three groups of alloys (Fig. 2). Note that AerMet 100 is comparable to Marage 250; AerMet 310 is comparable to Marage 300; and AerMet 340 is comparable to Marage 350. In addition, the titanium alloys have specific strengths similar to those of the AerMet 100 and 310 alloys. This gives designers a choice of three alloy types for a given specific strength level.

Ductility properties

Although the AerMet alloys, maraging steels, and titanium alloys have comparable specific strengths, their yield strengths differ considerably, as shown in Table 3. When the gap between yield and ultimate strengths is calculated and plotted as shown in Fig. 3, a major difference between the AerMet alloys and the other two groups emerges.

The titanium alloys and maraging steels generally have only an approximate 8 to 10 ksi difference between yield and ultimate strengths. However, the alloys in the AerMet family have a gap of approximately 35 to 40 ksi between yield and ultimate strengths.

This yield-to-ultimate strength range may explain one of the major differences among the three alloy families: the amount of ductility. Figures 4 and 5 show elongation and reduction in area for the titanium alloys, maraging steels, and AerMet alloys as a function of specific strength.

Observe that linear relationships exist for both the AerMet alloys and the maraging steels. The ductility measurements of the AerMet alloy family are superior to those of the maraging steels at any given strength. The two titanium alloys are intermediate between the steels, with the Ti-6Al-4V alloy showing better ductility than the Ti-10V-2Fe-3Al alloy.

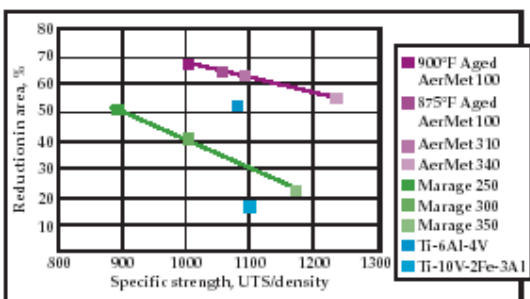


Fig. 5 — Reduction in area vs. specific strength.

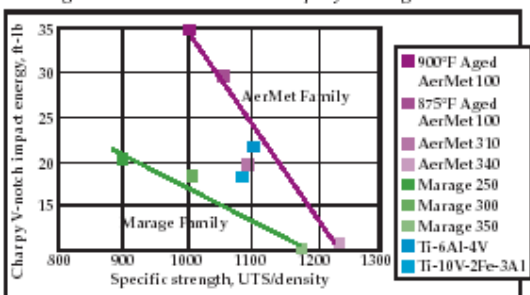


Fig. 6 — Comparison of Charpy V-notch impact energy vs. specific strength.

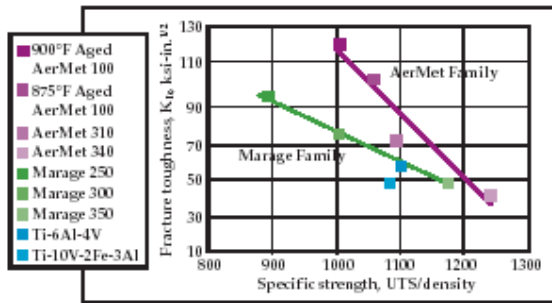


Fig. 7 – Fracture toughness vs. specific strength.

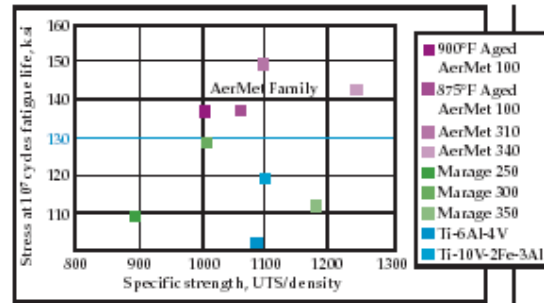


Fig. 8 – Rotating bending ($R = -1, K_t = 1$) fatigue life vs. specific strength.

Toughness measurements

When toughness is critical at very high strength levels, the AerMet alloy family appears to be a better choice than either the maraging steels or titanium alloys. Relative toughness is shown in Fig. 6, where Charpy V-notch impact energy is plotted against specific strength for the two high-strength steel families.

The plots show linear relationships for both the maraging steels and the AerMet alloys. The line for the AerMet alloys lies above and to the right of the line for the maraging steels, showing that for comparable strength levels, an AerMet alloy has superior impact properties. Again, the titanium alloys are superior to the maraging steels Fig. 6), but inferior to the AerMet alloys.

Similar linear relationships exist for fracture toughness as a function of specific strength, as shown in Fig. 7. Here, AerMet 100 and 310 have superior fracture toughness when compared with

Marage 250 and 300, respectively. At 350 ksi ultimate strength, AerMet 340 and Marage 350 have similar fracture toughness. At similar specific strength levels, the titanium alloys are inferior to the AerMet alloys.

When fatigue life is critical at very high strengths, the AerMet alloy family scores higher than both the titanium alloys and the maraging steels. The superior fatigue properties are seen when the stress at run-out is plotted against specific strength in Fig. 8.

This paper was written by Paul M. Novotny and Gernant E. Maurer, Carpenter Technology Corporation, Wyomissing, Pennsylvania. It was first published in Advanced Materials & Processes, November 2007 and is reprinted with permission of ASM International®. All rights reserved. www.asminternational.org

THE Cobalt Conference

Sheraton Centre Toronto, Canada • 14th-15th May 2008

There is still time to register for the conference but hurry, places are going fast!

And remember, you must make your hotel reservation before 13 April to get the special rate.

You can get the detailed schedule and programme at:

www.thecdi.com/conference

or contact Isabelle Porri, CDI on:

Tel: +44 (0)1483 510470 e-mail: iporri@thecdi.com

Nanoparticles unlock the future of superalloy metals

Sandia National Laboratories is pioneering the future of superalloy materials by advancing the science behind how those superalloys are made.

As part of Sandia's nanoscale research, a group of experts specializing in inorganic synthesis and characterization, modelling, and radiation science have designed a radical system of experiments to study the science of creating metal and alloy nanoparticles. Sandia is a National Nuclear Security Administration (NNSA) laboratory.

This research has vast implications, says Tina Nenoff, project lead. The lightweight, corrosion-resistant materials that the team is creating are needed for weapons casings, gas turbine engines, satellites, aircraft, and power plants.

"What we're doing is taking a completely new approach to thinking about producing superalloy materials," Nenoff says. "We're using radiation to break down the molecular structure of substances and form nanoparticles -- a synthetic approach that is flexible and versatile for making large quantities of superalloy nanoparticle compositions that can't be easily created otherwise."

A quick trip down memory lane to the days of high school science class will recall those chapters on material and chemical science defining alloys as a combination of two or more elements, at least one of which is a metal, where the resulting material has metallic properties different -- sometimes significantly different -- from the properties of its components. For instance, steel is stronger than iron, its primary component.

Superalloys, as the name would imply, stand out from the general population of alloys in the same way Superman would be considered extraordinary compared to the rest of us. These specialized alloys are exceptionally strong, lightweight, and able to withstand extremes that would destroy everyday metals like steel and aluminium.

"These high-performance superalloys are revered for their remarkable mechanical strength and their resistance to corrosion, oxidation, and deformation at high temperatures," says Jason Jones, Sandia researcher.

In the past, the development of these superalloys has depended on chemical and technological innovations, and been driven mainly by the aerospace and power industries where superalloys are in high demand.

"The method of radiation we're studying -- known as radiolysis -- introduces an entirely new area of research into creating alloys and superalloys through nanoparticle synthesis," Nenoff says. "This process holds promise as a universal method of nanoparticle formation. By developing our understanding of the basic material science behind these nanoparticle formations, we'll then be able to expand our research into other aspects of superalloys, like nickel-based alloys."

The team is focusing its research on studying the science that happens in the "novel metastable phase spaces" that are not accessible with traditional alloy production methods, such as melting, Nenoff says. These "phase spaces" are possible points in a given path, or orbit, that represent the motion of a particle over a period of time. Each potential state of that particle's system corresponds to one unique point in a phase space. Understanding these spaces is important for determining what alloys are created and how they form.

In the team's experiments, solvent molecules are combined with molecules or ions and dissolved in water, and the researchers then subject the solution to radiolysis. By varying the reaction conditions and using alcohols as agents to limit particle growth size, the researchers say they have determined through high-resolution transmission electron microscopy that they have been able to successfully grow particles that are nearly identical, delivering essentially defect-free superalloy metal nanoparticles.

The team of Sandia researchers perform these highly specialized experiments with the unique combination of the in-house Gamma Irradiation Facility (GIF) and the Ion Beam Materials Research Laboratory (IBMRL), which provide the radiation environments demanded by this research.

"The target solutions are placed in the testing cells at the GIF where they are exposed to a variety of gamma irradiation test configurations and controlled

radiation dose rates," says Don Berry, GIF supervisor. "High-intensity radioactive sources, which are kept submerged below 18 feet of deionised water to shield workers from radiation, are then raised via elevators into the testing cells to irradiate the targets. Once the irradiation is completed, the radioactive sources are returned to their shielded location in the water pool, and workers can again safely enter the cells."

In their study of the particle growth that takes place, the researchers expose the test solutions to even higher doses of radiation at the IBMRL.

"The ion beam irradiation experiments take place in a custom-built cell at the external beam end-station of the Tandem Van de Graff accelerator and result in intense dose rates in the solution," says ion beam researcher Jim Knapp. "A beam of protons exits the vacuum and passes through a thin Kapton film before entering into the target solution. The system can expose targets for up to several hours, but the exposures needed in these experiments are usually only fractions of a second."

After irradiation at the GIF or IBMRL, samples -- none of which are radioactive -- are studied using a variety of techniques, such as ultraviolet-visible spectroscopy and high-resolution transmission electron microscopy to understand what effects time and experimental variables have on particle formation, size, shape, and composition.

Depending on the combination of reactants, dose, and dose rate of radiation, researchers have been able to create nanometer-sized particles of gold in a variety of shapes including spheres, rods and pyramids.

Researchers are also translating the results of these experiments into computer simulations. Kevin Leung, Sandia researcher, is leading the effort to use ab initio molecular dynamics, along with other methods, to interpret and understand the controlling factors in the researchers' experiments.

"Using the results from the experiments, together with Sandia's world-class computational capabilities, we'll simulate the structure of the nanocrystal initiation," Leung says. "By examining the free energy present in the interface between the different materials, we will be able to understand what factors govern the size of these metal alloy nanocrystals. Modelling this region of the metastable phase space right after radiation has been applied promises to be a new and exciting area of research."

"What we're doing is really breaking ground in the fundamental research in the science of the formation of superalloy nanoparticles," Nenoff says. "This is really the new frontier in superalloys."

TIAX Licenses High-Performance Cathode Material to Vale Inco for Portable Power Applications

New Technology Overcomes Safety Issues of Lithium Nickelate to Offer Increased Battery Runtime in Laptops, Cellular Phones, and Other Consumer Electronics

TIAX, a technology processingSM company and leader in clean energy, chemicals, and appliance technologies, announced today that it has granted an exclusive license covering its high-energy, high-performance cathode material to Vale Inco Limited for use in portable power applications. Vale Inco is part of one of the world's top diversified mining companies and a leading producer of nickel.

The TIAX cathode is a lithium-nickel material that achieves 40 percent higher capacity than the current industry standard cathode material used in lithium-ion batteries. TIAX has manipulated the crystal structure of lithium-nickel to deliver superior capacity, excellent safety, long cycle life, and high performance over a broad range of power and temperature.

The TIAX lithium-nickel cathode material represents a critical breakthrough in battery technology. The nickelate class of lithium-ion materials has long held the promise of significant benefits in energy and power, but until now, the associated safety risks have made these materials inappropriate for consumer applications.

During a multi-year, multi-million dollar development effort, TIAX adapted quantum mechanical modelling techniques to stabilize the lithium-nickel crystal structure. As a result, the TIAX cathode material has an excellent safety profile, making it possible for consumers to access the performance benefits of this class of materials for the first time.

The specific terms of the agreement were not made public. TIAX is one of the largest independent R&D centres for lithium-ion batteries and will continue to work closely with Vale Inco to support its product development activities. TIAX will also continue development of next-generation nickel-class cathode materials.

In addition to portable applications, TIAX has adapted its material for implementation in the hybrid electric vehicle market where high power capability, high energy density, excellent safety, and long cycle life are important. TIAX has begun marketing licenses to its material for automotive applications, and being an ethically and socially responsible company.

For more information contact:
Twig Mowatt, TIAX LLC, (617) 498-7366
mowatt.twig@tiaxllc.com

The trade-offs and economics in functional grades

Functional grading offers useful combinations of wear resistance and fracture toughness in WC/Co composites, but can also involve more complex alloys and a greater variety of properties. While much of the European research on the subject has involved nitrogen-induced gradients in hardmetals, American investigators have taken a hard look at carbon gradients in tungsten carbide/cobalt (WC/Co) cemented carbides. At Utah University's Department of Metallurgical Engineering in Salt Lake City they've developed both a characterisation technique for properties and a mathematical model for the far-from-simple structural reactions. Both were the subjects of papers at the MPIF's 2007 Denver Conference.

In the first of these, Haibo Zhang of the University of Utah introduced the *Characterisation of functionally graded WC/Co composites using a Hertzian indentation technique*. Functionally graded materials (FGM) incorporated gradual engineered transitions in microstructure and/or composition, their greatest merit being to combine irreconcilable properties of materials in the same component, such as high fracture toughness with maximised wear resistance. For example, tough bulk and hard surface are requirements for mining picks, which are simultaneously subjected to severe shock and abrasive wear. However, quantitative evaluation of the mechanical properties of graded WC/Co

materials remained a challenge.

The author began by describing conventional methods for measuring the fracture toughness of homogeneous WC/Co – the Palmqvist indentation test, which evaluated the surface fracture toughness of the material, and an alternative standard based on plain strain fracture toughness. There were two variants of the latter, single-edge notched beam (SENB, ASTM E1304-89) and short bar/rod (ASTM B771-87), both of which needed a machined or ground notch in the surface. Neither directly measured the fracture toughness of functionally graded material, since they were intended for homogeneous material. A different method that could directly test the response of a graded microstructure was clearly desirable. In this investigation, the Hertzian indentation technique had been chosen to evaluate the toughness of FG WC/Co materials.

In the Hertzian test a specimen was loaded by a near-frictionless spherical indenter to deliver a normal load on a flat surface. Typically, two damage modes were generated, cone cracks if the indented material response

was "brittle" and plastic deformation beneath the contact circle if the indented material response was "tough". The Hertzian indentation technique had been extensively used to characterise multi-layered ceramics. It had been shown that this method was suitable for quasibrittle gradient ceramics with a certain layer thickness, such as $\text{Si}_3\text{N}_4/\text{Si}_3\text{N}_4+\text{BN}$. In the current investigation the plastic deformation of WC/Co materials had been studied with this technique. As well as providing indentation stress/strain curves, the "brittleness index" of the composite could be characterised and this index could be correlated with fracture toughness. Although Hertzian indentation was applied at the specimen surface, the volume tested extended into the bulk of material and therefore captured the mechanical response of its sub-surface layer. The mechanical responses of graded WC/Co were compared to those of homogeneous WC/Co with similar compositions.

A twin-layer WC/Co structure with coating thickness of 0.5mm was used in this study. Since conventional liquid-phase sintering was the most economical and convenient method to fabricate WC/Co

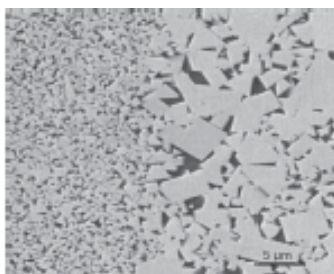


Figure 1. SEM micrograph of bilayer WC/Co.

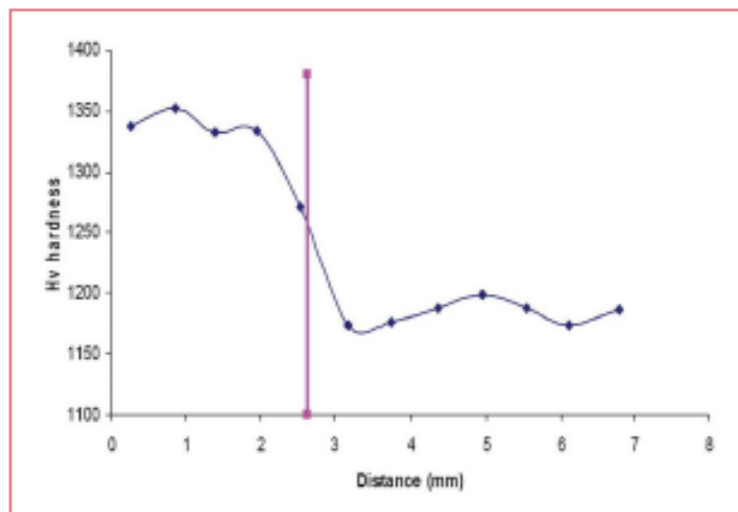


Figure 2. Hardness profile across the interface.

material, samples were fabricated by layer-to-layer stacking and cold pressing, followed by liquid-phase sintering.

Based on a previous study, the two components for the coating and substrate were chosen as 0.8 μ m WC/13Co and 5 μ m WC/10Co respectively. Target hardness of the former was about HV1400, acting as harder component or coating layer, whilst that of the latter was HV1200, representing the substrate.

Cobalt analysis

The mixed WC, cobalt and wax powders were stacked and cold-pressed in a compacting die, then sintered in a vacuum furnace at 1400°C for 60 minutes. After sintering, the parts were ground to the desired layer thickness and polished using 1 μ m diamond paste. Hardness tests were followed by cobalt analysis using EDAX equipment.

Hertzian indentations were made on the polished surfaces using a polycrystalline diamond (PCD) indenter sphere with a 5.08mm (0.2in) radius, considered rigid relative to the specimen. The PCD indenter had a Young's modulus of 850 GPa, whilst that of WC/Co is around 550 GPa. The servohydraulic test machine offered loads from 0.1 to 26.0kN, with a loading rate of 100 N/s. Measurements of contact radius a at each given load P were taken within one hour of indentation.

Earlier work had shown that, although elastic recovery caused the depth or profile of the residual impression to be different from that when fully loaded, the impression radius remained virtually unchanged. This meant that, after unloading, the contact radius could be used for calculation. After each indentation, the impression was examined by optical microscopy. The indenter was also examined for damage after each indentation and changed if necessary. From the measured contact radius, indentation stress and strain were calculated using p_0

equal to $P/\pi a^2$ and ϵ equal to a/R respectively.

In order to determine the load required to initiate quasi-plastic deformation (P_V), a Zygo optical profilometer was used to measure axial displacement along the loading direction after each load increase. When the displacement reached a preset value – when measured depth was greater than the amplitude of background signals, caused by the specimen's surface roughness – the corresponding load was designated the critical load for the onset of quasi-plastic deformation. To determine the load required to initiate fracture (P_C), the specimen was indented by an increasing series of loads and examined by light microscopy after each indentation. The load which visibly cracked at least a quarter-circle of the ring was designated the critical load for forming ring cracks.

To check for compositional and property gradients in the sintered WC/Co bilayer, the microstructure was examined by SEM, EDAX and other tests. The microstructure of sintered bilayer WC/Co is shown in Figure 1, the light phase being WC and the dark phase cobalt binder. EDAX analysis showed minimal Co migration during sintering, average cobalt content at the left side in figure 1 being about 12.9 per cent, on the right side about 10.2 per cent and at the interface about 11.7 per cent. The corresponding hardness gradient is illustrated in Figure 2.

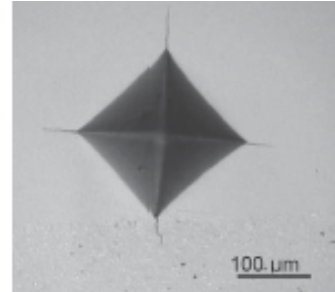


Figure 3. Vickers indentation at coating/substrate interface; diamond indenter, indentation load 50kgf.

Vickers impressions made at polished sections confirmed the intrinsic strength of interfaces (Figure 3). A key observation was the absence of delamination along the coating/substrate interface, implying that interface toughness was at least half that of the substrate material. Instead, the lower radial crack penetrated and was deflected by the tougher substrate.

After each indentation test, surface damage to the impression was observed using an optical microscope. When the indentation load was below a certain threshold value, the "sink in" phenomenon was observed. When the load exceeded the threshold, in addition to the "sink in", ring cracks and even radial cracks were found. Using the indentation load versus contact radius data, indentation stress and strain data were plotted as the stress-strain curve shown by Figure 4. Each data point represented an indentation, while the solid line was a regression fit of the data.

Indentation stress increased linearly versus indentation strain dur-

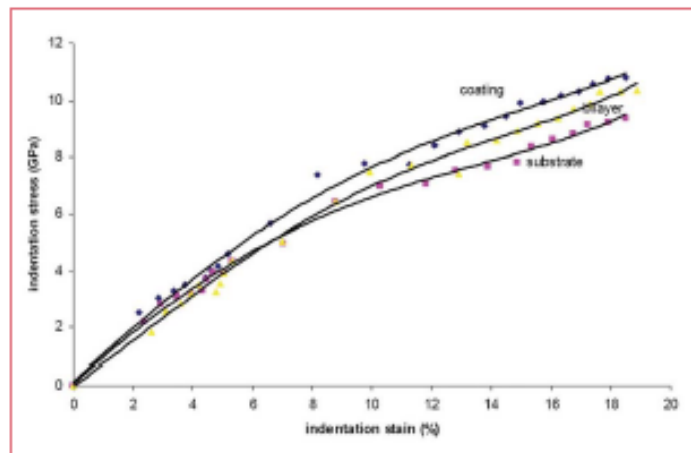


Figure 4. Indentation stress-strain curves for bilayer, coating and substrate. Data created with diamond indenter, indenter radius 5.08 mm.

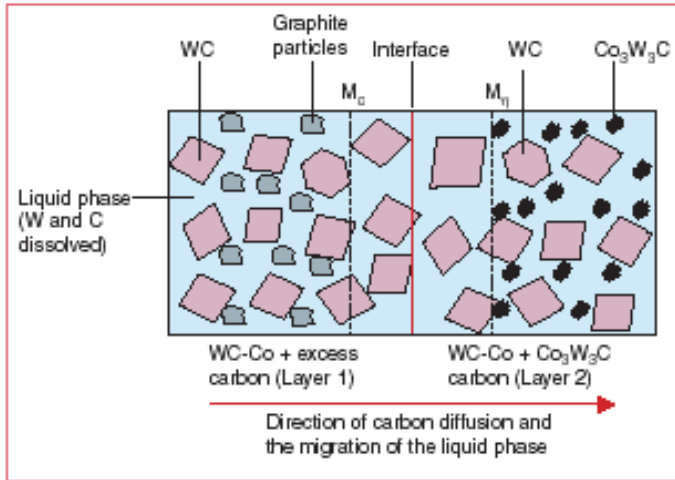


Figure 5. Schematic of cobalt gradient formation in a WC/Co bilayer during liquid phase sintering

ing the elastic stage, after which the curves deviated from linearity, indicating “yielding” behaviour. At high strain values, indentation stress levelled off even though strain continued to increase. This demonstrated that bilayer WC/Co exhibited quasi-plasticity and strain hardening.

At the same indentation strain, indentation stresses of the bilayer WC/Co were higher than the softer, tougher substrate, but lower than the harder coating layer. As a result, the author considered that, under the indentation load, functionally designed WC/Co performance would be an improvement over the individual constituents, being harder than the substrate but tougher than the hard but brittle coating layer.

The brittleness factor was investigated by further measurements from the Hertzian indentations. These were the load required to initiate fracture (P_C) and the load for onset of quasi-plastic deformation (P_Y). The so-called brittleness index was given by P_Y/P_C . For more brittle materials P_C was relatively low and P_Y relatively large, so the brittleness index P_Y/P_C (Ψ)

would also be large. For less brittle materials, P_Y/P_C would be much smaller. With the brittleness index, the behaviour of indented material could be simply predicted without damaging or destroying the whole sample.

The author’s measured brittleness indices of the materials in question are shown in Table 1. As expected, the brittleness index of bilayer WC/Co lay between those of the monolithic coating and tough substrate. From the engineering point of view, bilayer WC/Co not only acquired the wear resistance of the harder coating but also the toughness of the substrate.

The next related contribution approached the problems of functional gradient formation from a quite different angle, with *A kinetic model for cobalt gradient formation during liquid phase sintering of functionally graded WC/Co*. Though the University of Utah was again very much involved, it was presented by author Oladapo o. Eso of ATI Alldyne, Huntsville, Alabama.

The kinetic model was used to

describe the graded microstructure as a function of sintering time and temperature, as well as other factors including the volume fraction of Co_3W_3C (η) phase, liquid migration pressure and carbon content. The model predicted a decreasing rate of change of thickness of the WC/Co product layer, due to the phase reaction between carbon and η phase, with the volume fraction of η phase (f_η) in the sample and with the sintering time t . Good agreement was observed between the model and experimental results.

Finding a solution

The presenter’s introduction followed much the same lines as those of the previous paper discussed in this report. In summary, functionally graded WC/Co composites could provide a viable solution to the trade off in wear resistance and fracture toughness of WC/Co composites. An economic processing method for making these composites is liquid phase sintering, but migration of the liquid phase caused the cobalt content to even out during liquid phase sintering and, in a sample composed of two layers of WC/Co with different Co contents, the Co gradient was eliminated during liquid phase sintering. This was due to a driving force to decrease interfacial energy, based on a migration pressure gradient that depended on carbide particle size and the volume fraction of liquid.

During sintering, liquid phase migrated from a region with lower liquid migration pressure to a region with higher pressure. Redistribution continued until the liquid migration pressure was uniform everywhere in the WC/Co system, the migration velocity being proportional to the pressure gradient.

An important factor affecting liquid phase migration was carbon. An initial carbon gradient between two adjacent WC/Co layers prior to sintering resulted in a cobalt gradient after sintering. This was attributed to a combination of processes, including carbon diffusion, phase reaction and liquid

Table 1. Measured P_C and P_Y values for bilayer, coating and substrate with calculated brittleness index.

Sample	Critical load for ring crack P_C kN	Critical load for quasiplasticity P_Y kN	Brittleness index Ψ
Bilayer	14.0	0.18	0.013
Coating	11.5	0.20	0.017
Substrate	26.0	0.10	0.0038

migration, as illustrated in [Figure 5](#).

A bilayer specimen was prepared by pressing one layer of WC/Co containing excess carbon with another layer of WC/Co that was carbon deficient and therefore contained η phase at sintering temperature. Total carbon content was stoichiometric when the two layers were averaged. During sintering, graphite particles dissolved at one moving front (M_c) in layer one and dissolved carbon diffused through the liquid phase to react with the $\text{Co}_3\text{W}_3\text{C}$ particles at the other moving front (M_n) in layer two.

Diffusion of carbon in the liquid phase caused the migration of liquid phase in the same direction, due to the need to achieve equilibrium distribution. This was confirmed by thermodynamic calculations. A typical plot of the variation is shown in [Figure 6](#). Reaction between carbon and $\text{Co}_3\text{W}_3\text{C}$ particles produced metallic cobalt and altered the composition of the liquid phase.

Because the complex interactions between the different processes ([Figure 7](#)), including carbon diffusion, phase reaction and liquid migration, could create a cobalt gradient, the graded microstructure was non-equilibrium or metastable. Given enough time the gradient would be eliminated producing a homogenous composite. The kinetic rate of change was therefore a key factor in determining the transient cobalt gradient which, using typical sintering and cooling procedures, could be preserved down to room temperature.

The kinetics

Progressing through a logical sequence of equations (available in the published Conference Proceedings**), a model was developed to describe the kinetics of the process in terms of material variables (composition) and process variables (temperature and sintering time).

A Kennametal WC/10Co powder with $5\mu\text{m}$ average particle size

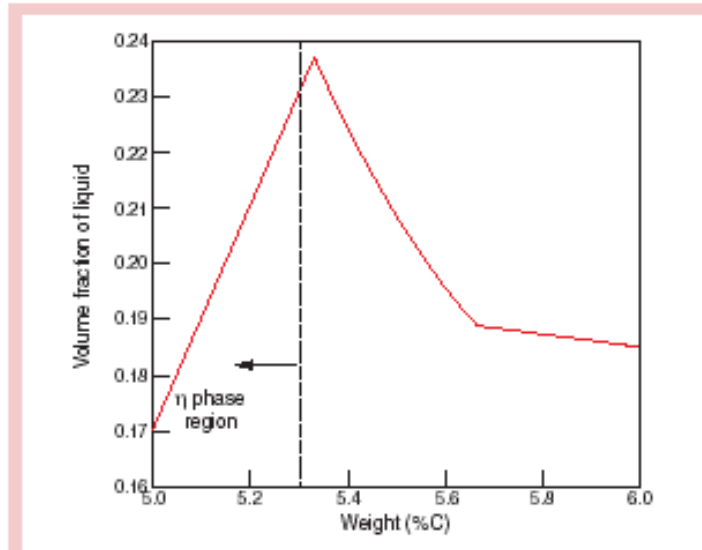


Figure 6. Calculated volume fraction of liquid as a function of total carbon content of WC/10Co at 1400°C .

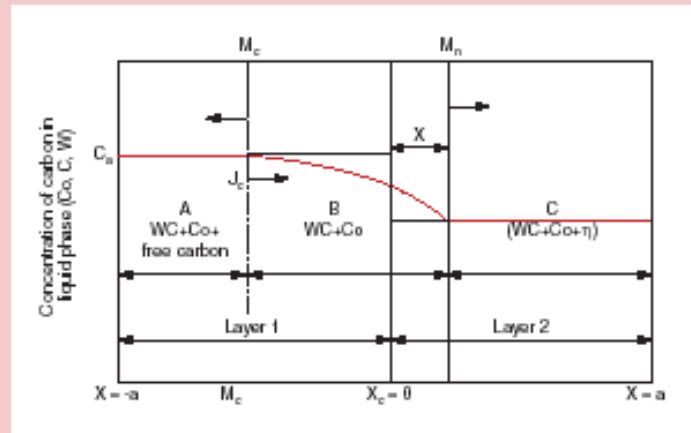


Figure 7. Different regions formed during sintering within a WC/Co bilayer having an initial carbon gradient.

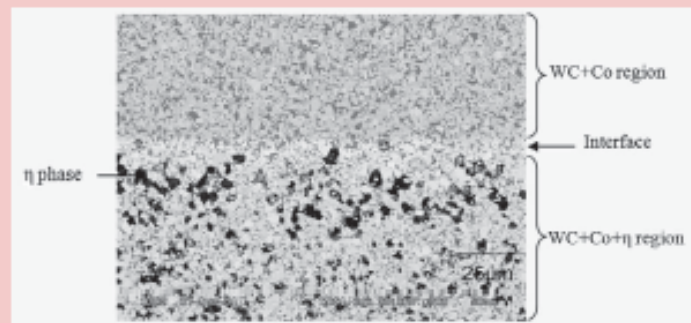


Figure 8. Scanning electron micrograph (back scattered electron mode) of a sintered WC/Co bilayer showing the interface between the WC (light grey) and Co (dark grey) and the WC+Co+ η (black) regions of the sample.

was the starting raw material for this study, powder composition being modified by adding graphite or tungsten powders to 200g batches of WC/10Co powder. The mixtures were milled in heptane in a bottle containing WC balls for 14 hours on a rolling mill, then dried at 80°C . Samples were compacted at 200 MPa into bilayer cylinders and dewaxed at

300°C . The calculated composition of each cylindrical sample is shown in [Table 2](#). Sintering experiments were carried out in a vacuum furnace with a heating rate of 10K/min. Samples were sintered at 1400°C for holding times of 15, 60, 120 and 180 minutes, furnace cooled, then polished and etched with Murakami's reagent for 10 seconds to exam-

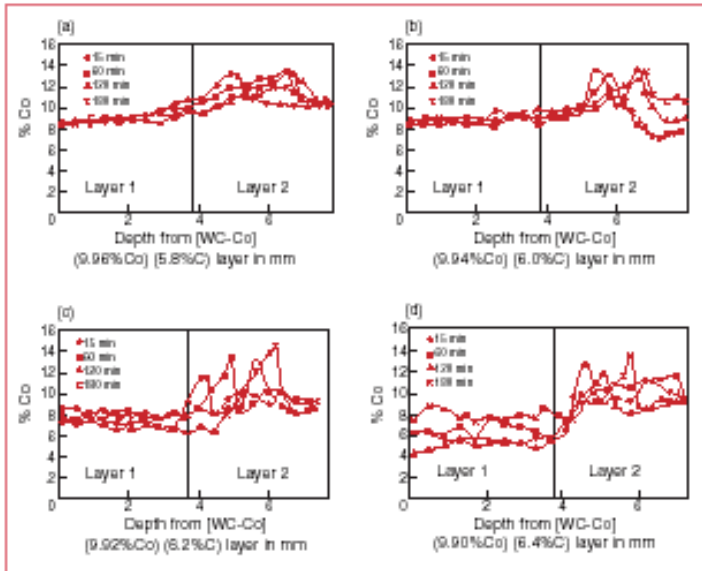


Figure 9. Cobalt distribution profile of a) Sample A, b) Sample B, c) Sample C, and d) Sample D, with initial compositions given in Table 1. The samples were sintered for different holding times (15, 60, 120 and 180 min) at 1400°C.

ine η phase and two minutes to examine tungsten carbide and cobalt phases. Cobalt distribution in the WC/Co bilayers was measured by energy dispersive spectroscopy (EDS) on a scanning electron microscope. Each data point on the cobalt distribution profile was generated by averaging EDS scans over an area 0.2 mm by 1.2 mm. The SEM micrograph of the WC+Co+ η region of the WC/Co bilayer (Figure 8) was converted to a binary image by giving the η darker contrast relative to the WC and Co phases. The area fraction of the η phase was then calculated by computer software. The WC grain size after sintering was measured by the linear intercept method.

Figure 9 shows that all the WC/Co bilayer samples in Table 1 developed a cobalt gradient after sintering at 1400°C for different holding times (15, 60, 120 and 180 minutes) at sintering temperature.

The presenter explained that the migration pressure of a WC/Co alloy could be calculated if the volume fraction of liquid phase at sintering temperature and the WC particle size were known. Calculated average grain size of WC in the sintered bilayer samples was 2.4 μ m. Migration pressure increased with the volume fraction of η phase, due to the reduction in the volume fraction of liquid

formed at the sintering temperature. However, the pressure increased with the volume fraction of liquid slightly above the stoichiometric carbon content and decreased as the volume fraction of liquid also decreased, due to graphite precipitation at higher carbon content. Precipitation of graphite caused volume expansion, resulting in the liquid phase being pushed away. The migration pressure gradient therefore increased with carbon gradient between the WC/Co layers, as shown in Figure 10.

Figure 11 compared and found good agreement between theoretical predictions (from the equations) and experimental results. Figure 12 plotted predicted values of characteristic diffusion distance L against sintering time. There was also good agreement be-

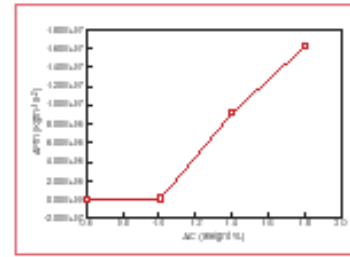


Figure 10. Variation of calculated migration pressure gradient as a function of carbon gradient between bilayer WC/Co samples in Table 2.

tween the model and the values of L obtained from SEM measurements. Diffusion distance increased with initial carbon gradient and sintering time.

This kinetic model predicted the position of the two moving boundaries as a function of material and processing parameters during the sintering of functionally graded WC/Co. The model demonstrated the relative importance of such material variables as carbon diffusivity, carbon concentration gradient, migration pressure gradient and volume fraction of η phase on process kinetics.

Liquid phase

Another parameter affecting the kinetics was the volume fraction of $\text{Co}_3\text{W}_3\text{C}$ (η) phase. An increase in initial carbon gradient between WC/Co layers did not affect the amount of carbon dissolved in the liquid phase within the carbon-rich WC/Co layer, because the liquid phase was already saturated with carbon at the sintering temperature.

However, the volume fraction of η phase (f_η) in the carbon-deficient

Table 2. Calculated compositions of WC/Co bilayers with different initial carbon gradients.

Sample	Layers	Initial cobalt content per cent	Initial total carbon content per cent	ΔC	Volume fraction of η phase (f_η)	η_{excess}
A	Layer 1	9.96	5.8	0.6	0.100	0.0225
	Layer 2	9.45	5.2			
B	Layer 1	9.94	6.0	1.0	0.161	0.0370
	Layer 2	9.09	5.0			
C	Layer 1	9.92	6.2	1.4	0.330	0.0511
	Layer 2	8.72	4.8			
D	Layer 1	9.90	6.4	1.8	0.528	0.0657
	Layer 2	8.36	4.6			

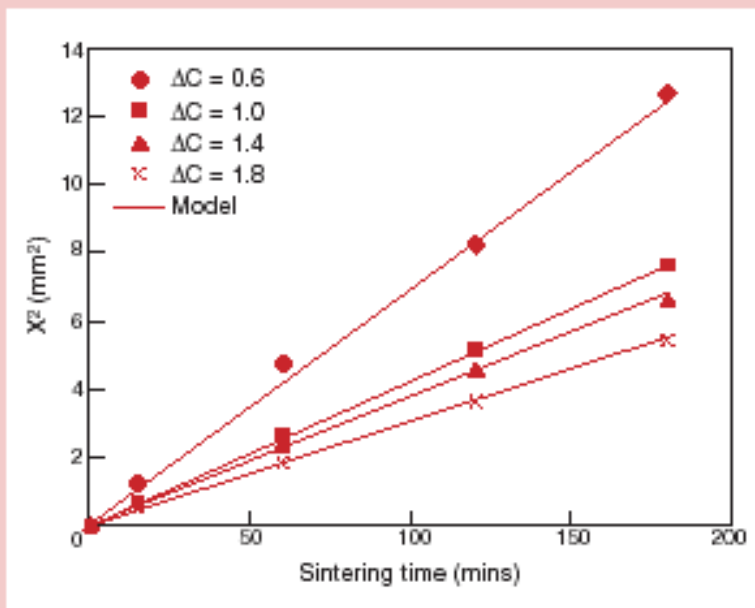


Figure 11. The predicted square of the WC/Co region thickness (X) as a function of sintering time.

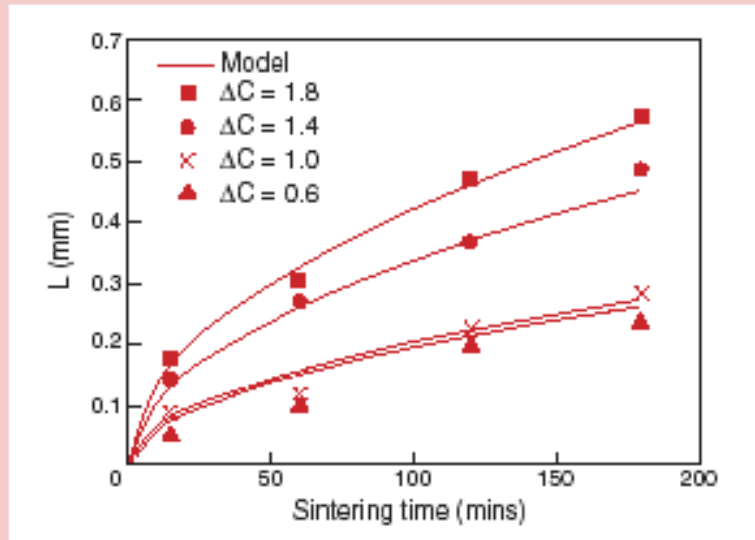


Figure 12. Predicted characteristic diffusion distance L as a function of sintering time.

WC/Co layer increased with the initial carbon gradient in the WC/Co bilayers. A higher volume fraction of η phase consumed more carbon. Hence an increase in volume fraction of η phase caused carbon to diffuse over longer distances to the surface of the η particles (Figure 10). In consequence, the rate of change of thickness of the WC/Co product layer (X) with sintering time, due to the phase reaction between carbon and η phase, decreased with volume fraction of η phase in the sample, as predicted by the kinetic model.

Conclusions

The author stressed the usefulness of comparing the assumptions on which the model was constructed with the real situation during liquid phase sintering. The model assumed constant carbon concentration and liquid migration pressure gradients. However, during the sintering process, carbon concentration and liquid migration pressure gradients were expected to vary with position within the specimen and with the sintering time. A study of the cobalt gradient formed in presin-

tered cemented carbide with deficient carbon after a carburising heat treatment showed a carbon gradient forming in the cobalt phase after the sample had cooled to room temperature. The measured carbon concentration profile showed a near-linear decrease in carbon concentration in the liquid phase, from the surface of the WC/Co sample saturated with carbon to a stable value in the inner layer containing phase. This indicated that the simplification of the carbon concentration profile in the liquid phase, as employed in this investigation, was valid.

The researchers were confident that the kinetic model developed in this study would be valuable in the design and manufacture of functionally graded WC/Co composites.

*** Advances in Powder Metallurgy & Particulate Materials – 2007, the Proceedings of the 2007 International Conference on Powder Metallurgy & Particulate Materials (Powder-Met2007) in Denver, USA, is published on CD-ROM in searchable Adobe Acrobat format by the Metal Powder Industries Federation, 105 College Road East, Princeton, NJ 08540-6692, USA. Phone: +1 609-452-7700, email: info@mpif.org, web: www.mpif.org*

This article is reprinted from Metal Powder Report, 62(11), Brookes K, The trade-offs and economics in functional grades, copyright 2007 with permission from Elsevier.